



HAL
open science

Quantitative atomic order characterization of a Mn₂FeAl Heusler epitaxial thin film

Samer Kurdi, Yuya Sakuraba, Keisuke Masuda, Hiroo Tajiri, Bhaskaran Nair,
Guillaume F Nataf, Mary Vickers, Günter Reiss, Markus Meinert, Sarnjeet
Dhesi, et al.

► **To cite this version:**

Samer Kurdi, Yuya Sakuraba, Keisuke Masuda, Hiroo Tajiri, Bhaskaran Nair, et al.. Quantitative atomic order characterization of a Mn₂FeAl Heusler epitaxial thin film. *Journal of Physics D: Applied Physics*, 2022, 55 (18), pp.185305. 10.1088/1361-6463/ac4e32 . hal-03585705

HAL Id: hal-03585705

<https://hal.science/hal-03585705>

Submitted on 14 Nov 2022

HAL is a multi-disciplinary open access archive for the deposit and dissemination of scientific research documents, whether they are published or not. The documents may come from teaching and research institutions in France or abroad, or from public or private research centers.

L'archive ouverte pluridisciplinaire **HAL**, est destinée au dépôt et à la diffusion de documents scientifiques de niveau recherche, publiés ou non, émanant des établissements d'enseignement et de recherche français ou étrangers, des laboratoires publics ou privés.

PAPER • OPEN ACCESS

Quantitative atomic order characterization of a Mn_2FeAl Heusler epitaxial thin film

To cite this article: Samer Kurdi *et al* 2022 *J. Phys. D: Appl. Phys.* **55** 185305

View the [article online](#) for updates and enhancements.

You may also like

- [Asymmetric Performance Testing of Carbon Felt Electrodes to Identify the Limiting Electrode in Vanadium Redox Flow Battery](#)
Ertan Agar, Christopher R. Dennison, Kevin W. Knehr et al.
- [Analysis of Irreversible Charge-Discharge Reaction in \$\text{LiFePO}_4/\text{Li}_4\text{Ti}_5\text{O}_{12}\$ Full-Cell Using Two-Phase Reaction Active Material](#)
Yuki Omote, Misaki Katayama and Yuki Orikasa
- [Analysis on the Electrochemical Series a.I. Chernomorskii Scientific Resources Co](#)
Alexandr I. Chernomorskii



The Electrochemical Society
Advancing solid state & electrochemical science & technology

242nd ECS Meeting

Oct 9 – 13, 2022 • Atlanta, GA, US

Abstract submission deadline: **April 8, 2022**

Connect. Engage. Champion. Empower. Accelerate.

MOVE SCIENCE FORWARD



Submit your abstract



Quantitative atomic order characterization of a Mn_2FeAl Heusler epitaxial thin film

Samer Kurdi^{1,8,*} , Yuya Sakuraba^{2,*} , Keisuke Masuda² , Hiroo Tajiri³,
Bhaskaran Nair¹, Guillaume F Nataf^{1,9} , Mary E Vickers¹, Günter Reiss⁴,
Markus Meinert⁵ , Sarnjeet S Dhesi⁶ , Massimo Ghidini^{1,6,7}  and Zoe H Barber¹

¹ Department of Materials Science and Metallurgy, University of Cambridge, CB3 0FS Cambridge, United Kingdom

² Research Center for Magnetic and Spintronics Materials, National Institute for Materials Science (NIMS), 1-2-1, Sengen, Tsukuba 305-0047, Japan

³ Center for Synchrotron Radiation Research, Japan Synchrotron Radiation Research Institute, 1-1-1 Kouto, Sayo, Hyogo 679-5198, Japan

⁴ Center for Spinelectronic Materials and Devices, Physics Department, Bielefeld University, D-33501 Bielefeld, Germany

⁵ Department of Electrical Engineering and Information Technology, Technical University of Darmstadt, Fraunhoferstraße 4, 64283 Darmstadt, Germany

⁶ Diamond Light Source, Chilton, Didcot, OX11 0DE Oxfordshire, United Kingdom

⁷ Department of Physics, Mathematics and Computer Science, University of Parma, 43130 Parma, Italy

E-mail: sk862@cantab.ac.uk and sakuraba.yuya@nims.go.jp

Received 17 October 2021, revised 10 January 2022

Accepted for publication 24 January 2022

Published 10 February 2022



CrossMark

Abstract

In this work, we investigate the effect of anti-site disorder on the half-metallic properties of a Mn_2FeAl Heusler alloy thin film. The film was grown on TiN-buffered MgO 001 substrates via magnetron sputtering. A detailed structural characterization using x-ray diffraction (XRD) and anomalous XRD showed that the film crystallizes in the partially disordered $L2_1B$ structure with 33% disorder between the Mn(B) and Al(D) sites. We measure a positive anisotropic magnetoresistance in the film, which is an indication of non-half metallic behaviour. Our x-ray magnetic circular dichroism sum rules analysis shows that Mn carries the magnetic moment in the film, with a positive Fe moment. Experimentally determined moments correspond most closely with those found by density functional calculated for the $L2_1B$ structure with Mn(B) and Al(D) site disorder, matching the experimental structural analysis. We thus attribute the deviation from half-metallic behaviour to the formation of the $L2_1B$ structure. To realize a half-metallic Mn_2FeAl film it is important that the inverse Heusler XA structure is stabilized with minimal anti-site atomic disorder.

⁸ Current address: Department of Quantum Nanoscience, Kavli Institute of Nanoscience, Delft University of Technology, Lorentzweg 1, 2628 CJ Delft, The Netherlands

⁹ Current address: GREMAN—UMR 7347, CNRS, Université de Tours, INSA CVL, 37000 Tours, France

* Authors to whom any correspondence should be addressed.



Original content from this work may be used under the terms of the [Creative Commons Attribution 4.0 licence](https://creativecommons.org/licenses/by/4.0/). Any further distribution of this work must maintain attribution to the author(s) and the title of the work, journal citation and DOI.

Supplementary material for this article is available [online](#)

Keywords: Heusler alloy, spintronics, x-ray absorption spectroscopy, x-ray diffraction, x-ray magnetic circular dichroism, spin polarization, thin films

(Some figures may appear in colour only in the online journal)

1. Introduction

Spin transport electronics, or simply spintronics [1] is a rapidly growing field that studies how to exploit the magnetic spins of electrons in addition to their charge. The field was invigorated in 1988 when Peter Grünberg [2] and Albert Fert [3] demonstrated the giant magnetoresistance (GMR) effect. Since then there have been many breakthroughs in the field, for example the hard disk drive with high storage capacity [4], magnetic random-access memory [5] and low power computing [6].

Half-metallic materials have a bandgap in one spin-orientation at the Fermi level and metallic behaviour in the other spin band [7], which results in the conduction of only one spin orientation, and hence a 100% spin polarized current. Half-metallic materials are therefore of great interest for spintronic devices, for example for enhancing the magnetoresistance in both magnetic tunnel junctions [8–12] and current-perpendicular-to-plane (CPP-GMR) devices [13–16]. Unfortunately, some of the raw elements of the various magnetic layers in available magnetic tunnel junctions and CPP-GMR devices have been identified as critical [17], and therefore it is crucial to investigate alternative materials made from readily available and cheaper elements [18, 19].

Heusler alloys are a group of intermetallic alloys [20] which provide a very promising framework to design new sustainable materials [19] to replace those currently used in spintronic devices. Elemental and composition tuning in Heusler alloys can lead to different types of magnetism [21], in addition to properties that are advantageous for enhancing the sensitivity of spintronics devices, such as half-metallicity [7].

Regarding half-metallic Heusler alloys, previous studies have focused on the Co-based Heusler alloys [22] and devices based on these alloys such as tunnelling magnetoresistance [12, 23–26] and CPP-GMR devices [14, 15, 27, 28]. However, Co is one of the elements that is considered critical [29]. Amongst half-metallic Heusler alloys comprised of only sustainable elements, Mn_2FeAl (inverse Heusler structure, XA, space group No. 216) is promising because of its predicted half-metallic behaviour [30] and low magnetization ($1 \mu_{\text{B}}/\text{f.u.}$) [31], allowing for the realization of sensitive and densely packed spintronic devices. However, the half-metallic behaviour in Heusler alloys is sensitive to anti-site disorders [32–36] and it is therefore important that careful characterization of the atomic disordering and its effect on the spin-polarization in Mn_2FeAl is carried out.

Current studies have focused on bulk polycrystalline Mn_2FeAl which was stabilized in the β -Mn structure [37, 38]. Mn_2FeAl Heusler thin films were successfully fabricated by growth using molecular beam epitaxy [39, 40]. Whilst Lv *et al* [40], suggest that their MBE grown Mn_2FeAl film has $D0_3$

disorder, no direct evidence is provided. Moreover, they suggest that the magnetic moment of their films decreases with $D0_3$ disorder, in contrast to the Slater-Pauling prediction [31].

In our work we show how anti-site disorder affects the half-metallic properties of a Mn_2FeAl . We directly confirm the structure and level of disorder in a Heusler Mn_2FeAl thin film, grown via magnetron sputtering, using a combination of both x-ray diffraction (XRD) and anomalous XRD [41]. We also present for the first time, x-ray magnetic circular dichroism characterization of Mn_2FeAl to determine the element-specific magnetic moments of Fe and Mn. We compare our experimental structural analysis and determined magnetic moments with theoretical predictions calculated by density functional theory. Our accurate quantification of the atomic order and Fe and Mn magnetic moments will allow for future optimization of Mn_2FeAl thin films with half-metallic character.

2. Experimental

All data presented in the main paper were obtained from a single sample: 20 nm thick Mn_2FeAl deposited on a 2 nm TiN-buffered MgO 001 substrate, and capped with a 1.5 nm Ti /1.5 nm TiN bilayer. Film deposition was carried out using DC/RF-magnetron sputter deposition in a UHV sputtering chamber built by BESTEC GmbH, with a base pressure below 1×10^{-8} Pa. During all deposition steps the substrate ($10 \times 10 \text{ mm}^2$) was rotated at 10 RPM to ensure homogeneous deposition across the surface. Film deposition took place at Ar or Ar/ N_2 (6 N) gas pressure of 0.2 Pa. The MgO 001 substrates were loaded directly from the supplier's (CrysTec GmbH) vacuum-sealed packaging.

The TiN buffer (2 nm) and cap (1.5 nm) were deposited at substrate temperature of 600 °C (using a radiative heater positioned at the back of the substrate holder) and room temperature, respectively, using reactive sputtering (RF-source), in mixed Ar/ N_2 sputtering gas (Ar flow = 10 sccm; $\text{N}_2 = 0.8$ sccm). The deposition rate was 0.01 nm s^{-1} and was in the fully poisoned regime [42] which indicates that the Ti target (99.995% purity) surface was covered with a nitride layer (supplementary note 1 available online at stacks.iop.org/JPhysD/55/185305/mmedia). The TiN buffer was chosen as its lattice parameter matches well ($\epsilon \sim 0.71\%$) with MgO (001) [43]. Furthermore, it resulted in better oriented and smoother Mn_2FeAl films (supplementary note 2).

The 20 nm Mn_2FeAl film was deposited at 450 °C from three individual DC targets: Fe (99.95% purity), Mn (99.9% purity) and Al (99.999% purity), at a total rate of $\sim 0.13 \text{ nm s}^{-1}$. The film was then capped with a 1.5 nm thick Ti film (RF-source) at room temperature (and 0.17 nm s^{-1}) to protect the

surface from N₂ bombardment during subsequent deposition of the TiN final cap.

The individual element deposition rates were first calibrated *in situ*, using a quartz crystal microbalance and confirmed by x-ray reflectivity (XRR) measurements (for Fe and Mn) and atomic force microscopy (AFM, Bruker MM8) (for Al). The composition of the film was then verified to be Mn_{2.02±0.01}Fe_{0.98±0.01}Al_{1.04±0.01} from a 600 nm-thick sample using energy dispersive x-ray analysis (EDX) in a Zeiss LEO 1530 scanning electron microscope with an Amptek X-123SDD EDX detector. A 15 keV voltage was used to obtain the *K* and *L* lines for quantification.

High resolution x-ray diffraction (XRD) was performed using a four-circle Panalytical Empyrean vertical θ/θ diffractometer with a hybrid 2-bounce primary monochromator. A proportional counter was used for the $2\theta/\theta$ and ω scans and a 2D PIXCEL position sensitive detector for collecting the reciprocal space maps (RSMs). A Bruker D8 4-axes diffractometer with a mirror to give a pseudo-parallel beam was used to obtain the φ -scans, the 200, 400 $2\theta/\theta$ scans without χ -offset and the 111, 220, 222 $2\theta/\theta$ scans with χ -offset (supplementary note 3) to calculate the ordering parameters. The experimental peak intensities were determined by profile fitting using HighScore+ software. The theoretical intensities were calculated as outlined in supplementary note 3. A Philips X'Pert Pro MPD θ/θ diffractometer was used to obtain the XRR scans.

The anomalous XRD (AXRD) measurements were performed at the BL13XU beamline using a six-circle diffractometer at SPring-8. To evaluate the atomic ordering in the Mn₂FeAl film, the 111 peak intensity (I_{111}) was measured at the Mn and Fe *K* absorption edges. Simulations of the I_{111} were performed from 6.3–6.7 keV for Mn and 7.0–7.3 keV for Fe assuming an *XA*-type Mn₂FeAl structure (figure 1(a)).

The x-ray adsorption spectroscopy and magnetic circular dichroism (XAS and XMCD) measurements were performed on the I06 beamline at the Diamond Light Source. The atomic magnetic moments were measured using total electron yield mode and the element specific hysteresis loops were measured using fluorescence detection. To determine the magnetic moments, the Mn and Fe $L_{3,2}$ edges were probed for parallel (I^+) and antiparallel (I^-) alignment of photon helicity with respect to a 2 T applied magnetic field at an angle 60° with respect to the sample normal. The XMCD signal ($I^+ - I^-$) was then analysed using the XMCD sum rules [44] to extract the overall magnetic moments of Fe and Mn and separate their orbital and spin contributions. In this work, 4.5 and 3.4 for the number of holes in the $3d$ band for Fe [45] and Mn [46] were used respectively. To remove intermixing complications between the Mn L_3 and L_2 edges, a 1.47 correction factor [47] was used to adjust the Mn spin moment.

To measure the anisotropic magnetoresistance (AMR), the Mn₂FeAl film was patterned into Hall-bar devices using photolithography followed by an Ar ion-milling step. A Quantum Design physical properties measurement system (PPMS DynaCool) was used to carry out the AMR measurement. A constant 1 mA DC current was applied and the magnetic field was rotated in the plane of the film.

We calculated the density of states (DOS) of ordered and disordered Mn₂FeAl using density functional theory (DFT) and the Korringa-Kohn-Rostoker (KKR) method [48, 49], implemented in the Akai-KKR software package [50]. The generalized gradient approximation was used for the exchange-correlation energy [51] and the disordered states were treated within the coherent potential approximation. The lattice parameters were set to $a = 5.948$ Å and $c = 5.776$ Å, determined via XRD. The Brillouin-zone integration was performed with $10 \times 10 \times 10$ k points. Under these conditions, we calculated the DOS of *XA*-ordered (figure 1(a)), L_2B -ordered (100% (Mn(A) \leftrightarrow Fe(C) disorder) (figure 1(b)), and other variations of disorder in Mn₂FeAl (table 1).

3. Results

The high resolution XRD characterization of the Mn₂FeAl film grown on a 2 nm TiN buffered MgO (001) substrate shows both the principal 400 reflection and the 200 superlattice reflection indicating a degree of *B2* ordering (figure 1(c)). Satellite peaks (thickness fringes) around the MgO (002) peak (indicated by the black arrows) stemming from the 2 nm TiN buffer layer are observed illustrating uniform buffer layer growth. To gain in-plane information about the film, a RSM of the 206 reflection was collected (figure 1(d)). To obtain accurate peak positions, the sample was aligned using the 224 peak of the MgO substrate. The out of plane, *c*, and in-plane, *a*, lattice parameters were calculated from the Mn₂FeAl reflections in figures 1(c) and (d) to be 5.776 ± 0.001 Å and 5.948 ± 0.001 Å respectively. The in-plane lattice constant, *a*, is larger than the out of plane lattice parameter, *c*, indicating tetragonal distortion due to strain induced by the lattice matching of the Mn₂FeAl film and the TiN buffer layer. There is a 45° in-plane rotation of the Mn₂FeAl lattice relative to the TiN buffer layer in order to achieve lattice matching ($a_{\text{TiN}} \approx a_{\text{Mn}_2\text{FeAl}} \cos 45^\circ$). To confirm this, a RSM was taken for a 40 nm thick TiN film (supplementary note 1), in which the in-plane lattice parameter calculated for the TiN film is 4.206 ± 0.001 Å, giving a lattice spacing of 5.948 ± 0.001 Å at a 45° in-plane rotation, matching the Mn₂FeAl in-plane lattice parameter.

An XRR scan (figure 1(e)) revealed Kiessig fringes over the entire 5° range for the 20 nm thick film. The roughness is determined to be ~ 0.55 nm from the scan simulation.

φ -scans from the Mn₂FeAl 220 and the MgO 220 reflections, shown in figure 1(f), confirm the in-plane 45° rotation of the Mn₂FeAl film relative to the TiN-buffered MgO substrate: (Mn₂FeAl(001)[110] || TiN(001)[100] || MgO(001)[100]). The φ -scans also confirm the presence of the 111 peak from the Mn₂FeAl film.

We have performed a quantitative analysis of the XRD patterns to determine the degree of *B2* and *XA* ordering [52] in the film, via the order parameters S_{B2} and S_{XA} respectively. S_{B2} was calculated as the average of the intensity ratios of the superlattice 002 and 222 reflections versus the fundamental 220 and 400 reflections respectively as:

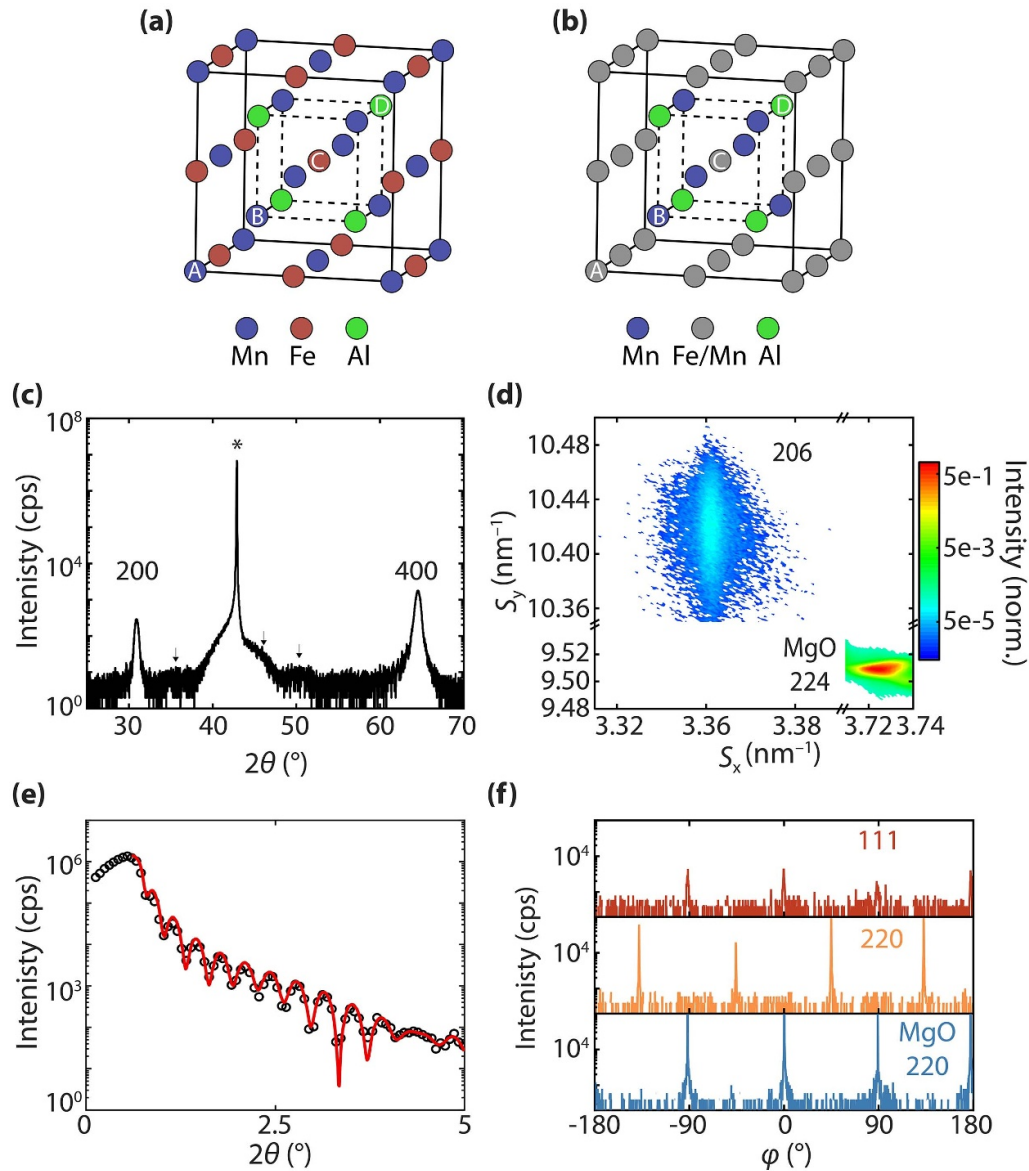


Figure 1. Structural characterization using x-ray diffraction (XRD). (a) *XA* and (b) *L*₂₁*B* Mn_2FeAl crystal structures. The A, B, C, and D sites correspond to 4a, 4c, 4b, and 4d Wyckoff positions respectively. (c) High resolution XRD $2\theta/\theta$ scan, * indicates the MgO 002 reflection and the grey arrows indicate the satellite peaks of the 2 nm TiN buffer layer. (d) Reciprocal space map of the Mn_2FeAl 206 and MgO 224 reflections. (e) X-ray reflectivity scan in which the open circles and the solid lines represent the measured and simulated curves respectively. (f) φ -scans of the MgO 220 (bottom), Mn_2FeAl 220 (middle) and 111 (top) reflections.

Table 1. Summary of the Mn_2FeAl structures and disorders studied in this work.

| | Structure | Disorder | Stoichiometry |
|-----|---|---|--|
| I | <i>XA</i> | n/a | $Mn_{1.0}Mn_{1.0}Fe_{1.0}Al_{1.0}$ |
| II | <i>L</i> ₂₁ <i>B</i> | $Mn(A) \leftrightarrow Fe(C)$ | $(Mn_{0.5}Fe_{0.5})Mn_{1.0} (Mn_{0.5}Fe_{0.5})Al_{1.0}$ |
| III | <i>D</i> 0 ₃ | $Mn(A,B) \leftrightarrow Fe(C)$ | $(Mn_{0.67}Fe_{0.33})(Mn_{0.67}Fe_{0.33})(Mn_{0.67}Fe_{0.33})Al_{1.0}$ |
| IV | <i>L</i> ₂₁ <i>B</i> with partial <i>B</i> 2 disorder | $L_{21}B + 33\%Mn(B) \leftrightarrow Al(D)$ | $(Mn_{0.5}Fe_{0.5})(Mn_{0.67}Al_{0.33})(Mn_{0.5}Fe_{0.5})(Al_{0.67}Mn_{0.33})$ |
| V | <i>L</i> ₂₁ <i>B</i> with partial <i>D</i> 0 ₃ disorder | $L_{21}B + 50\%Mn(B) \leftrightarrow Fe(A,C)$ | $(Mn_{0.75}Fe_{0.25})(Mn_{0.5}Fe_{0.5})(Mn_{0.75}Fe_{0.25})Al_{1.0}$ |
| VI | <i>L</i> ₂₁ <i>B</i> with partial <i>A</i> 2 disorder | $L_{21}B + 40\%Mn(A,C) \leftrightarrow Al(D)$ | $(Mn_{0.3}Fe_{0.5}Al_{0.2})Mn_{1.0}(Mn_{0.3}Fe_{0.5}Al_{0.2})(Al_{0.6}Mn_{0.4})$ |

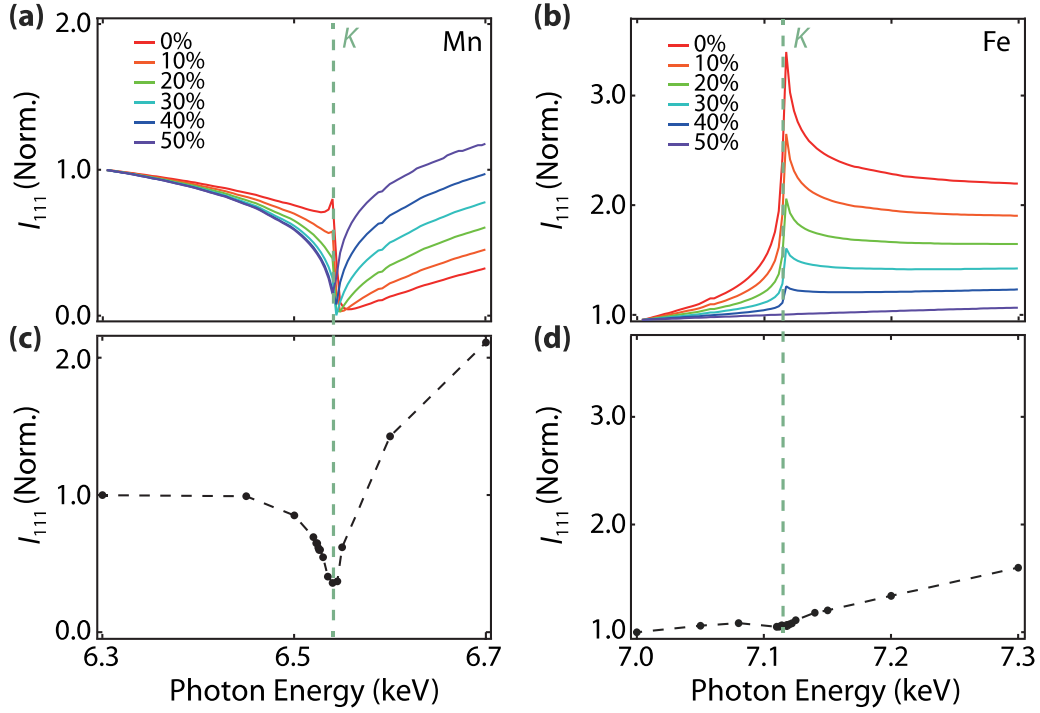


Figure 2. Confirmation of structure and ordering using anomalous x-ray diffraction (AXRD). Simulated AXRD 111 reflection intensity (I_{111}) of Mn_2FeAl in the XA structure as a function of $\text{Mn(A)} \leftrightarrow \text{Fe(C)}$ disorder from 0% to 50%, near the (a) Mn K -edge and the (b) Fe K -edge; (c) and (d) corresponding experimental data (filled black circles are the raw data and the dashed black lines are guides for the eyes only). The specific K -edges of both Mn and Fe are indicated by the dashed vertical green lines.

$$S_{B2}^2 = \frac{I_{\text{superlattice}}^{\text{measured}} / I_{\text{fundamental}}^{\text{measured}}}{I_{\text{superlattice}}^{\text{calculated}} / I_{\text{fundamental}}^{\text{calculated}}}. \quad (1)$$

S_{XA} was calculated from the average of the intensity ratios of the superlattice 111 reflections versus the fundamental 220 and 400 reflections as:

$$\left[S_{XA} \left(\frac{2 - S_{B2}}{2} \right) \right]^2 = \frac{I_{\text{superlattice}}^{\text{measured}} / I_{\text{fundamental}}^{\text{measured}}}{I_{\text{superlattice}}^{\text{calculated}} / I_{\text{fundamental}}^{\text{calculated}}}. \quad (2)$$

The reflection intensities were corrected by the Lorentz-Polarization factor and for geometrical effects which result from the changes in the x-ray and sample interaction volume with the χ -angle offset due to sample tilting (supplementary note 3). It is found that the degree of S_{B2} is larger than S_{XA} , 0.86 ± 0.17 and 0.29 ± 0.10 respectively. The implication of the calculated S_{B2} and S_{XA} on the actual atomic ordering in the film depends on whether the film crystallizes in the ordered inverse Heusler structure (XA), as predicted [31], or another structure with partial or full-disorder between Fe and Mn like the $L2_1B$ -Heusler structure.

Since Fe and Mn have similar scattering factors, it is challenging to determine the specific atomic ordering of our film using XRD [53]. If we were to analyse S_{L2_1B} in the same way as above, by using the XRD data, based on the $L2_1B$ structure shown in figure 1(b), we would get almost the same value as S_{XA} in the Mn_2FeAl film. Thus, to determine the

exact crystal structure including Fe and Mn ordering, we carried out AXRD experiments [41]. We first simulate the x-ray energy dependence on I_{111} at the Mn (figure 2(a)) and Fe (figure 2(b)) K absorption edges of XA -ordered Mn_2FeAl . By incrementing the amount of $\text{Mn(A)} \leftrightarrow \text{Fe(C)}$, we observe a change of the line shape of the simulated intensities, mainly the gradual change from convex upward to downward at the Mn K -edge and the suppression of the peak at the Fe K -edge. By comparing the experimentally obtained I_{111} AXRD data at the Mn (figure 2(c)) and Fe (figure 2(d)) K -edges with the simulated data, we verify a high degree of $\text{Mn(A)} \leftrightarrow \text{Fe(C)}$ disorder suggesting that the Mn_2FeAl film is not XA -ordered (figure 1(a)), but $L2_1B$ -ordered (figure 1(b)). In the $L2_1B$ structure, the Mn and Fe atoms share the $A(0,0,0)$ and $C(1/2, 1/2, 1/2)$ sites equally, unlike in the XA structure in which Mn atoms solely occupy the $A(0,0,0)$ site and Fe atoms solely occupy the $C(1/2, 1/2, 1/2)$ site. Moreover, recalling the order parameters, $S_{XA} \sim 0.29$ and $S_{B2} \sim 0.86$, determined by XRD, we can now also specify that this small value of S_{XA} results in 33% $\text{Mn(B)} \leftrightarrow \text{Al(D)}$ disorder ($B2$ -disorder) in the $L2_1B$ structure as verified by the Takamura model [52].

XAS and XMCD measurements were performed to determine both the atomic magnetic moments of Mn (figures 3(a) and (b)) and Fe (figures 3(c) and (d)) and to measure element-selective hysteresis loops, at 1.5 K (figure 3(e)). Figure 3(e), reveals that Mn has the larger magnetic moment compared to Fe. This is further supported by the sum-rules-derived magnetic moments summarized in table 2, in which the total Mn

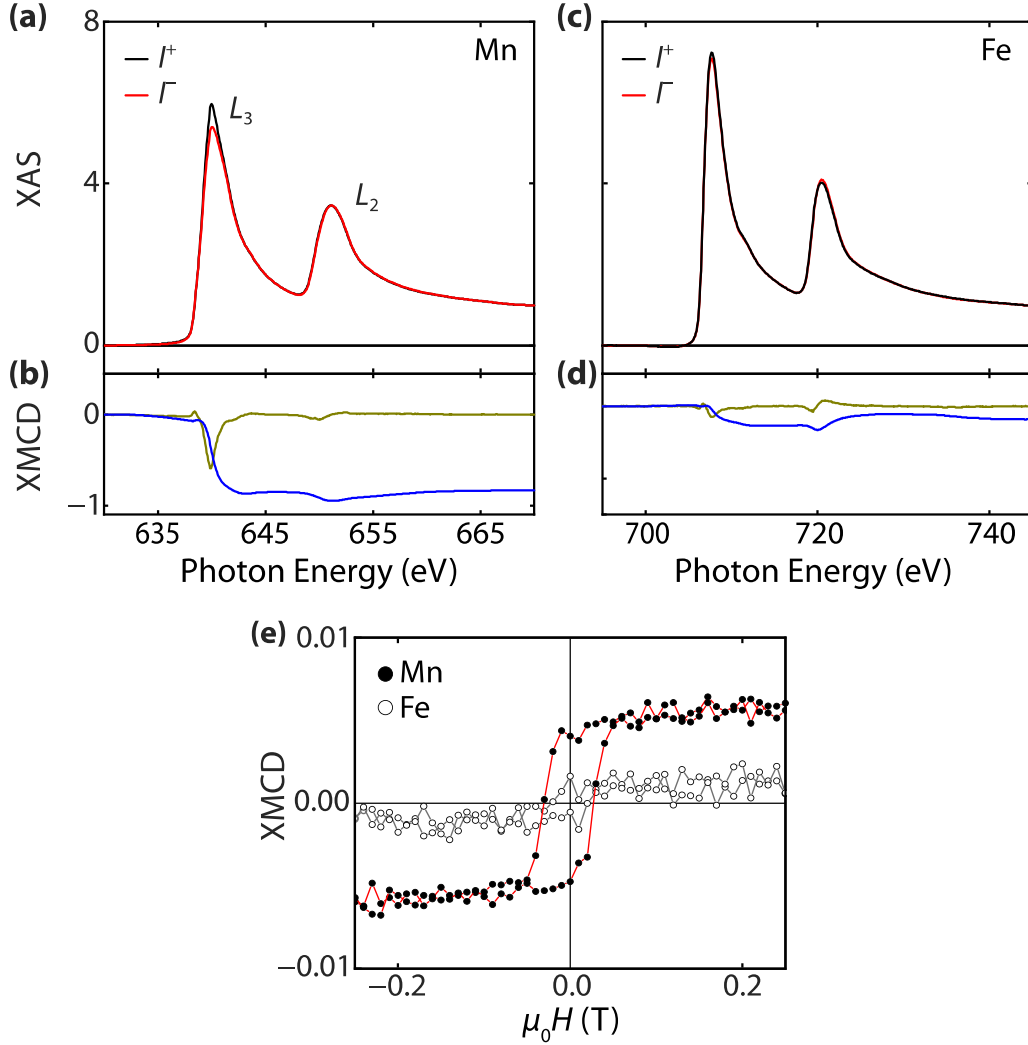


Figure 3. X-ray adsorption spectroscopy and circular magnetic dichroism (XAS and XMCD) spectra and element specific hysteresis loops. Averaged XAS spectra for the (a) Mn (six scans) and the (c) Fe (eight scans) L_2 and L_3 absorption edges. The XAS spectra were measured with right (black) and left (red) circularly polarized light. The corresponding averaged XMCD spectra for (b) Mn and (d) Fe. XMCD spectrum (green) and the integral of the XMCD spectrum (blue). The spectra were taken at $T = 1.5$ K in a 2 T applied magnetic field. (e) XMCD element selective hysteresis loops for Fe (open circles) and Mn (filled circles) measured at $T = 1.5$ K and saturated to ± 2 T – points were only collected to ± 0.25 T. Points and solid lines represent raw data.

Table 2. Summary of the XMCD sum rule analysis for the Mn_2FeAl film as a function of temperature (m_{spin} , m_{orb} and m_{tot} (μ_B) denote the measured spin, orbital and total magnetic moments respectively).

| | | 150 K | 100 K | 50 K | 1.5 K |
|----|------------|-------------------|-------------------|-------------------|-------------------|
| Mn | m_{spin} | 0.087 ± 0.019 | 0.085 ± 0.017 | 0.11 ± 0.03 | 0.18 ± 0.04 |
| | m_{orb} | 0.012 ± 0.005 | 0.020 ± 0.008 | 0.03 ± 0.01 | 0.06 ± 0.03 |
| | m_{tot} | 0.099 ± 0.020 | 0.105 ± 0.021 | 0.14 ± 0.04 | 0.24 ± 0.05 |
| Fe | m_{spin} | 0.071 ± 0.028 | 0.060 ± 0.030 | 0.077 ± 0.059 | 0.061 ± 0.006 |
| | m_{orb} | 0.024 ± 0.002 | 0.005 ± 0.005 | 0.029 ± 0.028 | 0.017 ± 0.010 |
| | m_{tot} | 0.095 ± 0.040 | 0.065 ± 0.035 | 0.106 ± 0.076 | 0.078 ± 0.009 |

and Fe moments in Mn_2FeAl at 1.5 K are $0.48 \pm 0.10 \mu_B$ and $0.078 \pm 0.009 \mu_B$, respectively. The Fe moment is too small to be strictly analysed in this study, which results in large error in our sum rules calculations, nevertheless it is shown to be smaller relative to the Mn moment up to a temperature of 150 K (table 2).

To probe the half-metallic behaviour of the Mn_2FeAl , an AMR measurement was conducted. Figure 4 plots the AMR ratio vs. the in-plane angle (φ) with respect to the 100 axis for the Mn_2FeAl film at 30 K, in which clear two-fold symmetric curves are observed. The AMR ratio is shown to be positive which indicates that the film does not have half-metallic

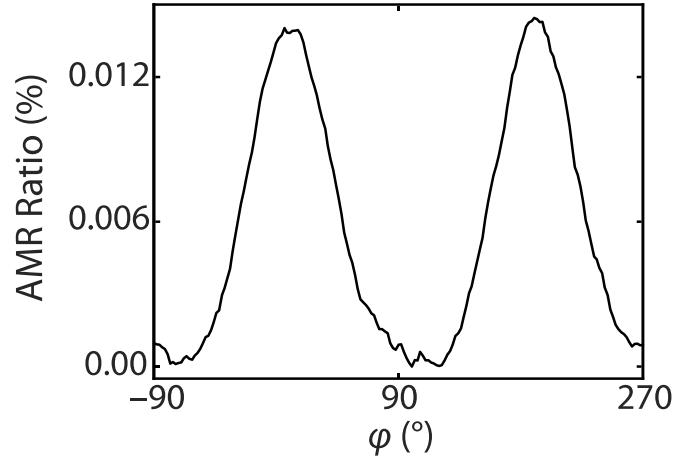


Figure 4. Anisotropic magnetoresistance (AMR). Dependence of the AMR ratio on the relative in-plane angle between the DC current and external magnetic field, φ , in the Mn_2FeAl epitaxial films at 30 K.

character as it has been previously shown that a negative AMR ratio is an indication of half-metallic character in Heusler alloy films [54–56]. Although we expect some shunting of the electric current in the TiN buffer layer, it does not affect the positive sign of the AMR we observed as the positive sign of the AMR is an intrinsic property of the Mn_2FeAl film.

4. Theoretical calculations and discussion

Atomic order in Heusler alloys significantly affects their electronic structure and their properties [32–36]. To elucidate the role of ordering towards the destruction of the half-metallic character of our Mn_2FeAl film, as verified by our AMR measurement, we calculated the spin-resolved DOS for the XA structure (figure 5(a)), the $L2_1B$ (figure 5(b)) structure, the $D0_3$ structure (figure 5(c)) and $L2_1B$ with various type of disorder (figures 5(d)–(f)). We summarize the corresponding spin polarization values in figure 5(g).

The total DOS for the XA -structure (figure 5(a)) shows a bandgap at the Fermi-energy (E_F) in the spin-down states (red) and a peak in spin-up state (blue), which is indicative of a large spin polarization and half-metallic character. Using the definition of the spin polarization: $P(\%) = D_\uparrow - D_\downarrow / D_\uparrow + D_\downarrow$, where D_\uparrow and D_\downarrow are the spin-up and spin-down DOS at E_F respectively, we calculate $P_{XA} = 94\%$. In contrast, for the DOS for the $L2_1B$ structure (figure 5(b)), the peak at E_F in the spin-up state is not present, and the gap in the spin-down state is reduced. We calculate the spin polarization to be 78% for the $L2_1B$ structure, suggesting that the Mn_2FeAl is no longer a half-metal although having a pseudo-gap structure. We also calculate the DOS of our film structure as verified by both AXRD and XRD: $L2_1B$ structure with partial $B2$ disorder (figure 5(d)). We find that this 33% $\text{Mn(B)} \leftrightarrow \text{Al(D)}$ disorder has a minimal effect on the spin polarization, giving 77%.

We then consider other combinations of disorder that are difficult to quantify using XRD due to the similar structure factors of Mn and Fe: figure 5(c) illustrates $D0_3$ disorder (perfect $\text{Mn(A,B)} \leftrightarrow \text{Fe(C)}$ disorder shown as III in table 1), figure 5(e) $L2_1B$ + partial $D0_3$ disorder (V in table 1) and figure 5(f) $L2_1B$ + partial $A2$ disorder (VI shown in table 1). These disorders result in a suppression of the spin polarization further: 8.7%, -34% and 2% respectively.

Lastly, in figure 5(h) we compare our XMCD-determined Fe and Mn moments with the calculated moments of the structures shown in figures 5(a)–(f) (figure 5(h)). We show that the $D0_3$ disordered structure, namely the XA structure with $\text{Mn(A,C)} \leftrightarrow \text{Al(D)}$ disorder that was reported by Lv *et al* [40], results in an enhancement of the magnetization of Mn_2FeAl due to the strong enhancement of the Fe moment. This is in conflict with their report of a magnetization which is smaller than $1 \mu_B/\text{f.u}$ due to calculation of the magnetic moment assuming only the XA structure.

Our AXRD data clearly indicate that our Mn_2FeAl film has 100% $\text{Mn(A)} \leftrightarrow \text{Fe(C)}$ disorder ($L2_1B$ structure). However, since the ideal $L2_1B$ structure shows a negative Fe moment (figure 5(h)), which was not observed in our XMCD experiments, we consider how the Mn and Fe moment changes with additional atomic disorder in the $L2_1B$ structure. We exclude both the partial $D0_3$ disorder ($\text{Mn(B)} \leftrightarrow \text{Fe(C)}$) and $A2$ disorder ($\text{Mn(A,C)} \leftrightarrow \text{Al(D)}$) which show a large enhancement of the Fe moment compared to our XMCD-calculated Fe moment. However, the $\text{Mn(B)} \leftrightarrow \text{Al(D)}$ disorder, which was confirmed via our XRD measurements, results in the reversal of the Fe moment, and matches the theoretical values of the XMCD-determined Mn and Fe moments most closely. Moreover, because the $L2_1B$ + partial $B2$ disorder ($\text{Mn(B)} \leftrightarrow \text{Al(D)}$) has non-half-metallic electronic structure, with a calculated spin polarization of 77%, we can conclude that this disordered state agrees well with our experimental observations.

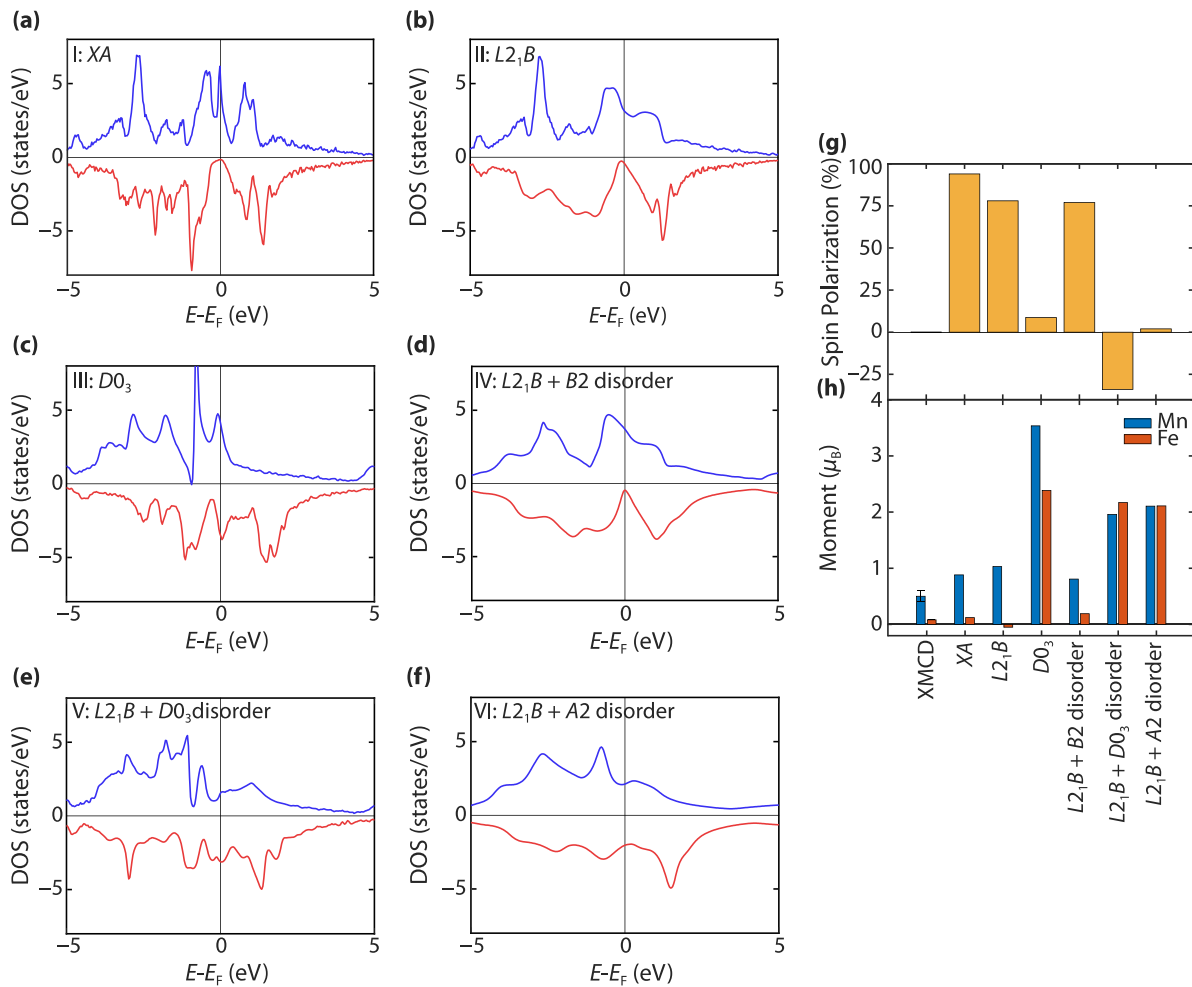


Figure 5. Density functional theory calculations and spin polarization. Spin resolved total density of states (DOS) for perfectly ordered Mn_2FeAl (a) XA ; (b) $L2_1B$, and (c) DO_3 . (d) $L2_1B$ + partial $B2$ disorder (33% $Mn(B) \leftrightarrow Al(D)$), (e) $L2_1B$ + partial DO_3 disorder (50% $Mn(B) \leftrightarrow Fe(A,C)$), and (f) $L2_1B$ + partial $A2$ disorder (40% $Mn(A,C) \leftrightarrow Al(D)$). The blue/red curves indicate the up/down spins. (g) Calculated spin polarization values, and (h) experimental (XMCD, at 1.5 K) and calculated Fe and Mn elemental magnetic moments for structures (a)–(f).

5. Conclusion

In summary, we investigated the effect of anti-site disorder on the half-metallic properties of epitaxially grown Mn_2FeAl thin film. Our AMR measurements confirm that the film is not a half-metal, which is supported by our DFT calculations that revealed the destruction of half metallicity in $L2_1B$ -ordered Mn_2FeAl . Our XMCD measurements reveal a small positive Fe moment and the Mn and Fe moments match best with the high resolution XRD and AXRD determined structure: $L2_1B$ Heusler structure, with 33% $Mn(B) \leftrightarrow Al(D)$ disorder. In order to use Mn_2FeAl as an environmentally friendly alternative ferromagnet for spin valve devices, it is important that the XA structure is realized with minimal disorder.

Data availability statement

All data that support the findings of this study are included within the article (and any supplementary files).

Acknowledgments

This work was funded by H2020-MSCA-ITN-2014 SELECTA (Grant Agreement No. 642642 of the European Commission), and Grants-in-Aid for Scientific Research (No. 17H06152) from the Japan Society for the Promotion of Science (JSPS), the 2019 NIMS internship program. G F N thanks the Royal Commission for the Exhibition of 1851 for support through the award of a Research Fellowship. We thank Diamond Light Source and SPring-8 for time on beamlines I06 (proposal SI18932) and BL13XU (proposal 2019A0927) respectively. The authors would like to thank Dr Niklas Teichert, Dr Edouard Lesne and Dr Martin Gottschalk for useful discussions and N Kojima for technical support.

Author contributions








S K, Y S, S S D, M G and Z H B conceived the experiments. S K, Y S, H T, B N, G F N and M G performed the experiments. S K, Y S, K M, H T, B N, M E V, G R, M M, S S D, and M G

modelled and analysed the data. All co-authors contributed to the written text with main contributions by S K, Y S and Z H B.

Conflict of interest

There are no conflicts to declare.

ORCID iDs

Samer Kurdi  <https://orcid.org/0000-0002-7374-2844>
 Yuya Sakuraba  <https://orcid.org/0000-0003-4618-9550>
 Keisuke Masuda  <https://orcid.org/0000-0002-6884-6390>
 Guillaume F Nataf  <https://orcid.org/0000-0001-9215-4717>
 Markus Meinert  <https://orcid.org/0000-0002-7813-600X>
 Sarnjeet S Dhesi  <https://orcid.org/0000-0003-4966-0002>
 Massimo Ghidini  <https://orcid.org/0000-0002-1905-2455>

References

- [1] Bader S D and Parkin S S P 2010 Spintronics *Annu. Rev. Condens. Matter Phys.* **1** 71
- [2] Binasch G, Grunberg P, Saurenbach F and Zinn W 1989 Enhanced magnetoresistance in layered magnetic structures with antiferromagnetic interlayer exchange *Phys. Rev. B* **39** 4828
- [3] Baibich M N, Broto J M, Fert A, Van Dau F N, Petroff F, Eitenne P, Creuzet G, Friederich A and Chazelas J 1988 Giant magnetoresistance of (001)Fe/(001)Cr magnetic superlattices *Phys. Rev. Lett.* **61** 2472
- [4] Fontana R E, Hetzler S R and Decad G 2012 Technology roadmap comparisons for TAPE, HDD, and NAND flash: implications for data storage applications *IEEE Trans. Magn.* **48** 1692
- [5] Apalkov D, Dieny B and Slaughter J M 2016 Magnetoresistive random access memory *Proc. IEEE* **104** 1796
- [6] Torrejon J et al 2017 Neuromorphic computing with nanoscale spintronic oscillators *Nature* **547** 428
- [7] de Groot F and Mueller R A 1981 New class of materials: half-metallic ferromagnets *Phys. Rev. Lett.* **50** 2024
- [8] Moodera J S, Kinder L R, Wong T M and Meservey R 1995 Large magnetoresistance at room temperature in ferromagnetic thin film tunnel junctions *Phys. Rev. Lett.* **74** 3273
- [9] Kämmerer S, Thomas A, Hütten A and Reiss G 2004 Co₂MnSi Heusler alloy as magnetic electrodes in magnetic tunnel junctions *Appl. Phys. Lett.* **85** 79
- [10] Bowen M, Bibes M, Barthélémy A, Contour J P, Anane A, Lemaître Y and Fert A 2003 Nearly total spin polarization in La_{2/3}Sr_{1/3}MnO₃ from tunneling experiments *Appl. Phys. Lett.* **82** 233
- [11] Sakuraba Y, Nakata J, Oogane M, Ando Y, Kato H, Sakuma A, Miyazaki T and Kubota H 2006 Magnetic tunnel junctions using B2-ordered Co₂MnAl Heusler alloy epitaxial electrode *Appl. Phys. Lett.* **88** 022503
- [12] Moges K, Honda Y, Liu H X, Uemura T, Yamamoto M, Miura Y and Shirai M 2016 Enhanced half-metallicity of off-stoichiometric quaternary heusler alloy Co₂(Mn,Fe)Si investigated through saturation magnetization and tunneling magnetoresistance *Phys. Rev. B* **93** 134403
- [13] Pratt W P, Lee S F, Slaughter J M, Loloee R, Schroeder P A and Bass J 1991 Perpendicular giant magnetoresistances of Ag/Co multilayers *Phys. Rev. Lett.* **66** 3060
- [14] Iwase T, Sakuraba Y, Bosu S, Saito K, Mitani S and Takanashi K 2009 Large interface spin-asymmetry and magnetoresistance in fully epitaxial Co₂MnSi/Ag/Co₂MnSi current-perpendicular-to-plane magnetoresistive devices *Appl. Phys. Express* **2** 06003
- [15] Jung J W, Sakuraba Y, Sasaki T T, Miura Y and Hono K 2016 Enhancement of magnetoresistance by inserting thin NiAl layers at the interfaces in Co₂FeGa_{0.5}Ge_{0.5}/Ag/Co₂FeGa_{0.5}Ge_{0.5} current-perpendicular-to-plane pseudo spin valves *Appl. Phys. Lett.* **108** 102408
- [16] Nakatani T, Sasaki T T, Sakuraba Y and Hono K 2019 Improved current-perpendicular-to-plane giant magnetoresistance outputs by heterogeneous Ag-In: Mn-Zn-O nanocomposite spacer layer prepared from Ag-In-Zn-O precursor *J. Appl. Phys.* **126** 173904
- [17] European Commission 2014 *Report on Critical Raw Materials for the EU, Report of the Ad Hoc Working Group on Defining Critical Raw Materials* (available at: https://ec.europa.eu/growth/sectors/raw-materials/areas-specific-interest/critical-raw-materials_en)
- [18] Kurdi S, Ghidini M, Divitini G, Nair B, Kursumovic A, Tiberto P, Dhesi S S and Barber Z H 2020 Exchange-bias via nanosegregation in novel Fe_{2-x}Mn_{1+x}Al ($x = -0.25, 0, 0.25$) Heusler films *Nanoscale Adv.* **2** 2602
- [19] Hirohata A et al 2017 Development of antiferromagnetic Heusler alloys for the replacement of iridium as a critically raw material *J. Phys. D: Appl. Phys.* **50** 443001
- [20] Heusler F 1903 Über magnetische manganlegierungen *Verh. Dtsch. Phys. Ges.* **12** 219
- [21] Graf T, Felser C and Parkin S S P 2011 Simple rules for the understanding of Heusler compounds *Prog. Solid State Chem.* **39** 1
- [22] Galanakis I, Dederichs P H and Papanikolaou N 2002 Origin and properties of the gap in the half-ferromagnetic Heusler alloys *Phys. Rev. B* **66** 134428
- [23] Sakuraba Y, Hattori M, Oogane M, Ando Y, Kato H, Sakuma A, Miyazaki T and Kubota H 2006 Giant tunneling magnetoresistance in Co₂MnSi/Al-O/Co₂MnSi magnetic tunnel junctions *Appl. Phys. Lett.* **88** 192508
- [24] Scheike T, Sukegawa H, Furubayashi T, Wen Z, Inomata K, Ohkubo T, Hono K and Mitani S 2014 Lattice-matched magnetic tunnel junctions using a Heusler alloy Co₂FeAl and a cation-disorder spinel Mg-Al-O barrier *Appl. Phys. Lett.* **105** 242407
- [25] Kämmerer S, Heitmann S, Meyners D, Sudfeld D, Thomas A, Hütten A and Reiss G 2003 Room-temperature preparation and magnetic behavior of Co₂MnSi thin films *J. Appl. Phys.* **93** 7945
- [26] Tsunegi S, Sakuraba Y, Oogane M, Takanashi K and Ando Y 2008 Large tunnel magnetoresistance in magnetic tunnel junctions using a Co₂MnSi Heusler alloy electrode and a MgO barrier *Appl. Phys. Lett.* **93** 112506
- [27] Sakuraba Y, Izumi K, Iwase T, Bosu S, Saito K, Takanashi K, Miura Y, Futatsukawa K, Abe K and Shirai M 2010 Mechanism of large magnetoresistance in Co₂MnSi/Ag/Co₂MnSi devices with current perpendicular to the plane *Phys. Rev. B* **82** 094444
- [28] Nakatani T M, Furubayashi T, Kasai S, Sukegawa H, Takahashi Y K, Mitani S and Hono K 2010 Bulk and interfacial scatterings in current-perpendicular-to-plane giant magnetoresistance with Co₂Fe(Al_{0.5}Si_{0.5}) Heusler alloy layers and Ag spacer *Appl. Phys. Lett.* **96** 212501
- [29] European Commission 2017 *Communication from the Commission to the European Parliament, the Council, the European Economic and Social Committee and the Committee of the Regions on the 2017 List of Critical Raw Materials for the EU* (available at: <https://eur-lex.europa.eu/legal-content/EN/TXT/?uri=CELEX:52017DC0490>)

- [30] Luo H Z, Zhang H W, Zhu Z Y, Ma L, Xu S F, Wu G H, Zhu X X, Jiang C B and Xu H B 2008 Half-metallic properties for the Mn_2FeZ ($Z=Al, Ga, Si, Ge, Sb$) Heusler alloys: a first-principles study *J. Appl. Phys.* **103** 083908
- [31] Skaftouros S, Özdoğan K, Şaşıoğlu E and Galanakis I 2013 Generalized Slater-pauling rule for the inverse Heusler compounds *Phys. Rev. B* **87** 024420
- [32] Raphael M P, Ravel B, Huang Q, Willard M A, Cheng S F, Das B N, Stroud R M, Bussmann K M, Claassen J H and Harris V G 2002 Presence of antisite disorder and its characterization in the predicted half-metal Co_2MnSi *Phys. Rev. B* **66** 104429
- [33] Miura Y, Nagao K and Shirai M 2004 Atomic disorder effects on half-metallicity of the full-Heusler alloys $Co_2(Cr_{1-x}Fe_x)Al$: a first-principles study *Phys. Rev. B* **69** 144413
- [34] Galanakis I, Özdoğan K, Aktaş B and Şaşıoğlu E 2006 Effect of doping and disorder on the half metallicity of full Heusler alloys *Appl. Phys. Lett.* **89** 042502
- [35] Picozzi S, Continenza A and Freeman A J 2004 Role of structural defects on the half-metallic character of Co_2MnGe and Co_2MnSi Heusler alloys *Phys. Rev. B* **69** 094423
- [36] Hülsen B, Scheffler M and Kratzer P 2009 Thermodynamics of the Heusler alloy $Co_{2-x}Mn_{1+x}Si$: a combined density functional theory and cluster expansion study *Phys. Rev. B* **79** 094407
- [37] Gavrikov I, Seredina M, Zheleznyy M, Shchetinin I, Karpenkov D, Bogach A, Chatterjee R and Khovaylo V 2019 Magnetic and transport properties of Mn_2FeAl *J. Magn. Magn. Mater.* **478**, 55
- [38] Dash S, Lukoyanov A V, Nancy, Mishra D, Rasi U P M, Gangineni R B, Vasundhara M and Patra A K 2020 Structural stability and magnetic properties of Mn_2FeAl alloy with a β -Mn structure *J. Magn. Magn. Mater.* **513** 167205
- [39] Lv B, Lian Z, Miao Y, Gao C, Si M, Xue D, Yu F and Yao J 2020 Realization of a Heusler alloy Mn_2FeAl with $B2$ ordering *Appl. Phys. Lett.* **116** 132404
- [40] Lv B, Liu P, Miao Y, Lian Z, Si M and Gao C 2021 Disorder effect of 3d transition elements in $D0_3$ Heusler alloy Mn_2FeAl *Appl. Phys. Lett.* **118** 132408
- [41] Ravel B, Cross J O, Raphael M P, Harris V G, Ramesh R and Saraf L V 2002 Atomic disorder in Heusler Co_2MnGe measured by anomalous x-ray diffraction *Appl. Phys. Lett.* **81** 2812
- [42] Berg S and Nyberg T 2005 Fundamental understanding and modeling of reactive sputtering processes *Thin Solid Films* **476** 215
- [43] Niesen A, Glas M, Ludwig J, Schmalhorst J-M, Sahoo R, Ebke D, Arenholz E and Reiss G 2015 Titanium nitride as a seed layer for Heusler compounds *J. Appl. Phys.* **118** 243904
- [44] Chen C T, Idzerda Y U, Lin H J, Smith N V, Meigs G, Chaban E, Ho G H, Pellegrin E and Sette F 1995 Experimental confirmation of the x-ray magnetic circular dichroism sum rules for iron and cobalt *Phys. Rev. Lett.* **75** 152–5
- [45] Elmers H J et al 2003 Element-specific magnetic moments from core-absorption magnetic circular dichroism of the doped Heusler alloy $Co_2Cr_{0.6}Fe_{0.4}Al$ *Phys. Rev. B* **67** 104412
- [46] Klaer P, Balke B, Alijani V, Winterlik J, Fecher G H, Felser C and Elmers H J 2011 Element-specific magnetic moments and spin-resolved density of states in $CoFeMnZ$ ($Z = Al, Ga, Si, Ge$) *Phys. Rev. B* **84** 144413
- [47] Edmonds K W, Farley N R S, Johal T K, Van Der Laan G, Champion R P, Gallagher B L and Foxon C T 2005 Ferromagnetic moment and antiferromagnetic coupling in $(Ga,Mn)As$ thin films *Phys. Rev. B* **71** 064418
- [48] Korringa J 1947 On the calculation of the energy of a Bloch wave in a metal *Physica* **13** 392
- [49] Kohn W and Rostoker N 1954 Solution of the Schrödinger equation in periodic lattices with an application to metallic lithium *Phys. Rev.* **94** 1111
- [50] Akai H *AkaiKKR (MACHIKANEYAMA)* (available at: <http://kkr.issp.u-tokyo.ac.jp>)
- [51] Perdew J P, Burke K and Ernzerhof M 1996 Generalized gradient approximation made simple *Phys. Rev. Lett.* **77** 3865
- [52] Takamura Y, Nakane R and Sugahara S 2009 Analysis of L_{21} -ordering in full-Heusler Co_2FeSi alloy thin films formed by rapid thermal annealing *J. Appl. Phys.* **105** 07B109
- [53] Balke B, Wurmehl S, Fecher G H, Felser C, Alves M C M, Bernardi F and Morais J 2007 Structural characterization of the Co_2FeZ ($Z=Al, Si, Ga, and Ge$) Heusler compounds by x-ray diffraction and extended x-ray absorption fine structure spectroscopy *Appl. Phys. Lett.* **90** 172501
- [54] Yang F J, Sakuraba Y, Kokado S, Kota Y, Sakuma A and Takanashi K 2012 Anisotropic magnetoresistance in $Co_2(Fe,Mn)Si$ Heusler epitaxial films: a fingerprint of half-metallicity *Phys. Rev. B* **86** 020409(R)
- [55] Sakuraba Y, Kokado S, Hirayama Y, Furubayashi T, Sukegawa H, Li S, Takahashi Y K and Hono K 2014 Quantitative analysis of anisotropic magnetoresistance in Co_2MnZ and Co_2FeZ epitaxial thin films: a facile way to investigate spin-polarization in half-metallic Heusler compounds *Appl. Phys. Lett.* **104** 172407
- [56] Kokado S, Tsunoda M, Harigaya K and Sakuma A 2012 Anisotropic magnetoresistance effects in Fe, Co, Ni, Fe 4N, and half-metallic ferromagnet: a systematic analysis *J. Phys. Soc. Japan* **81** 024705